Verification and Validation study of URANS simulations for axial waterjet propelled large high-speed ship

Tomohiro Takai, Manivannan Kandasamy, and Frederick Stern

IIHR – Hydroscience &Engineering,

The University of Iowa, C. Maxwell Stanley Hydraulics Laboratory,

Iowa City, IA 52242, USA

Abstract: The accurate prediction of waterjet propulsion using CFD is of interest from the standpoint of performance analyses of existing waterjet designs as well as improving and design optimization of new waterjet propulsion systems for high-speed marine vehicles. The present work is performed for three main purposes; i.e., 1) to investigate the capability of URANS flow solver, CFDSHIP-IOWA, to the accurate prediction for waterjet propelled simulation including the waterjet-hull interactions; 2) to carry out detailed verification and validation (V&V) analysis; and 3) to identify the optimization opportunity for intake duct shape design. A concentrated effort is applied to V&V work and performance analysis of waterjet propelled simulations which form the focus of this paper. The joint high speed sealift design (JHSS), which is a very large high-speed ship concept operating at a transit speed of at least 36 knots using four axial flow waterjets, is selected for the initial geometry on current work and subsequent optimization study. For self-propelled simulations, the ship accelerates until the resistance equals the prescribed thrust and added tow force and converges to the self propulsion point. Quantitative V&V studies are performed on both barehull and waterjet appended design with corresponding EFD data from the 1/34 scale model testing. Uncertainty assessments are performed on iterative convergence and grid size. As a result, total resistance coefficient for barehull case and self propulsion point for waterjet propelled case are validated at the average uncertainty intervals of 7.0%D and 1.1%D, respectively. Predictions of CFD computations capture the general trend of resistance over the speed range of 18-42knots, and show reasonable agreement with EFD within the average errors of 1.8%D and 8.0%D for barehull and waterjet case, respectively. Furthermore, results show that URANS is able to accurately predict the major propulsion related features such as volume flow rate, inlet wake fraction, and net jet thrust with an accuracy of ~9%D. The flow feature details inside the duct and interference of the exit jets are qualitatively well-predicted as well. It is found that there are significant losses on inlet efficiency over the speed range; hence, an objective for subsequent optimization study can be set to maximizing the inlet efficiency. Overall, V&V work has proved that the present approach is an efficient and accurate tool to predict the waterjet propelled JHSS and paved way of the optimization opportunity. The main objective of the optimization will be reduction of powering requirements by increasing the inlet efficiency through modification of intake duct shape.

Keyword: Waterjet propelled simulation – URANS CFD – Dynamic overset grids – V&V analysis – Waterjet-hull interactions

1. Introduction

Over the past decades, a variety of mechanical propulsion systems for marine vehicle, such as conventional screw propeller, controllable-pitch propeller, contra-rotating propeller, and waterjets (WJ), has been proposed. Nowadays, there is a growing interest in waterjet propulsion because it has a lot of benefits over conventional screw propeller such as shallow draft design, smooth engine load, less vibration, lower water borne noise, no appendage drag, and good maneuverability. In addition, waterjet has good efficiency over the required speed range because they are effective by recovering a part of the frictional drag by ingesting the low momentum boundary layer at inlets. These advantages have combined to increase the demand of waterjet propulsion systems for a variety of marine vehicles including high-speed naval sealift. Recently, significant advancements in waterjet technology have been made particular in two areas; compact waterjet technology and capability of computational fluid dynamics (CFD) for design and analysis. The current waterjet market is dominated mainly by the mixed-flow system; however, high-speed ships generally use slender hull forms to reduce the wave drag and require efficient propulsion system. Therefore, the axial-flow waterjet system, which is compact compared to mixed-flow systems, was introduced (for instance, Lavis *et al.*, 2006). For the same inlet diameter and the same unit thrust, the axial-flow pump has a significant smaller transom footprint than the mixed-flow pump.

The powering performance analysis of waterjet appended hulls using tow tank model testing has been a recent, ongoing area of research. The ITTC Waterjet Performance Prediction Specialist Committee (Van Terwisga, 2005) has developed a model testing procedure for waterjet propulsion. The committee adopted a control volume approach balancing momentum and energy through the waterjet system to arrive at system thrust, thrust deduction, and delivered power. The ITTC standard locations for the flow through the waterjet are illustrated in Figure 1. The inflow capture area is designated as Station 1(1a), one pump diameter ahead of the inlet tangency. Station 3 is located just ahead of the pump, and Station 6 is at the nozzle discharge. A suitable control volume needs to be selected for the waterjet system in order to be able to compute or determine the powering characteristics, and the control volume is defined by the stream-tube captured in between St. 1a and 6.

Wilson *et al.*, (2005) presented waterjet propulsion thrust results for a slender, high-speed hull form model propelled with four side-by-side waterjet units (Fn=0.511). It provided experimental and numerical results for realistic estimates of model scale propulsion interaction factors and the scaling of these results to full scale. Computational studies were carried out using a free-surface capable potential flow code. Jessup *et al.,* (2007) conducted model tests for the joint high speed sealift (JHSS) powered with four compact high density axial flow waterjet. The JHSS is a very large, high-speed ship concept (approximately 980ft long) for transport of a single Marine Brigade to overseas theaters. Tests were conducted with detailed starboard side LDV surveys at St. 1, 3,

and 6. Static wall pressure was measured at these stations. This approach relied heavily on LDV surveys to best document the flow non-uniformities at each station, with the use of wall static taps to establish the pressure across the station planes. To accurately measure jet velocity, testing incorporated all of the approaches explored by the ITTC. These included LDV surveys, bollard tests, single total head probes, and direct measure using weight scales. JHSS model testing data was selected as the validation test case as extensive data is available together with uncertainty assessments. JHSS is a mono-hull concept ship, has unique "gooseneck" bow which actually emerges above the free surface when the model is at rest. Main particulars and lines of JHSS barehull design are shown in Figure 2.

Recent innovations in CFD and high performance computing have enabled faster and cost effective approach for predicting waterjet propulsive characteristics. This has enabled detailed analysis of the flow through the waterjet ducts, which would require prohibitively expensive Laser Doppler Velocimetry (LDV) measurements if the whole flow field has to be measured. Such detailed flow analysis is required for a deeper understanding of the flow physics giving insights into further improvement of the performance characteristics of the waterjet. However, the CFD has to be thoroughly validated before relying on it for performance analysis, design, and optimization.

Bulten (2006) performed a detailed investigation both experimentally and numerically on a waterjet test setup where the waterjet inlet was mounted on top of a cavitation tunnel. The mass flow rate in the tunnel was adjusted to get the desired inlet velocity ratio (IVR) values. This was modeled in the CFD using a prescribed velocity profile at the inlet of the cavitation tunnel and a constant pressure boundary condition at the outflow plane. The waterjet stator and rotor geometry was also modeled. Validation demonstrated that the standard two equation turbulence model in combination with wall functions was able to predict the non uniformities in the duct flow field with acceptable accuracy. The results showed that the main inlet flow characteristics such as cavitation inception at cutwater where the flow to the duct separates from the main flow, velocity distribution at the impeller plane, flow separation at the inlet, the shape of the inlet stream tube are related to the IVR. The author recommends that a dedicated inlet design is recommended for each ship since variations in design ship speed and power density of the installations cause the design IVR to vary. The analysis of waterjet for the use of amphibian vehicle was performed by Jang *et al*., (2004) to provide detail understanding of complicated three-dimensional viscous flow phenomena including interactions of intake duct, rotor, stator, and contracted discharge nozzle. RANS flow solver with moving, non-orthogonal multi-block grid system was used. The CFD results were compared with experimental fluid dynamics (EFD) and the complex viscous flow feature of the waterjet, such as the secondary flow inside of the intake duct, the recovery of axial flow by the action of the stator, and tip vortex were predicted. The performance prediction of waterjet for the use of similar vehicle by diameter sizes and weights were investigated both numerically and experimentally by Kim *et al*., (2009).

An extensive study was undertaken to analyze the effect of integrating RANS calculations into experimental waterjet powering prediction by Delaney *et al.*, (2009). Two different JHSS models were considered; each model houses either axial-flow or mixed-flow waterjet. The hull, waterjet inlets, and shafts were modeled in

the simulation. Multi-element unstructured grids and boundary layer prism elements were generated around waterjet geometry. The free surface was treated as a symmetry plane, and the ship was modeled at sinkage and trim prescribed by the propelled experiment. RANS simulation used experimentally determined volumetric flow rates through the pump as a condition for the thrust provided by the actuator disk model. The effects of on the flow field non-uniformity were explored. The full scale simulations (Fn=0.35, Rn=5.3×10^9) were also performed in order to investigate the scaling effects by comparing boundary layers. The simulations results were discussed in particular on St 1 and 3; and RANS and EFD delivered pump power predictions showed good agreement with EFD within one percent at model scale and within two percent at full scale. Hino *et al.,* (2009) performed RANS analysis of a free surface flow around waterjet propelled high-speed ship (Fn=1.0, Rn=1.0×10^6). Free surface location was predicted using single-phase level set approach. An actuator disk model in which duct geometry is modeled in a computational grid was used to simulate the self-propelled condition. The nozzle shape was not modeled, and dynamic motions were not predicted. The flow fields of waterjet propelled simulations, such as free surface elevations, pressure distributions in the duct center planes, and limiting streamlines on a ship were compared with the towed simulations; however, the detailed V&V results were not given.

The present work is performed for three main objectives; namely, 1) to investigate the capability of URANS flow solver to the accurate prediction for waterjet propelled simulation including the waterjet-hull interactions; 2) to carry out detailed verification and validation (V&V) analysis; and 3) to identify the optimization opportunity for intake duct shape design. In the present work, computational setup differs from previous studies in that the waterjet-hull interactions and waterjet-wake interactions are also predicted with free surface and dynamic motions. The effects of waterjet-hull interaction are highly non-linear as they include the effect of the dynamic trim on boundary layer ingestion and shape of inflow stream tube, together with the effect of the waterjet induced vertical forces on the dynamic motion. Also, the shape of the ingested boundary layer is non-uniform over the entire cross-section at the inlet and it depends on the hull form. This phenomenon affects the non-uniformity of the flow inside the duct and hence affects the inlet efficiency. The waterjet-wake interactions do not significantly affect the propulsion characteristics, but are of interest in the study of wake signatures. Self propulsion simulations are carried out at model scale with an added tow force to compensate for the extra drag due to thicker boundary layer at model scale to get thrust loading similarity. In short, simulations are conducted using added tow force to match full-scale thrust identity. An actuator disk model is used inside the duct instead of modeling the impeller, as the latter requires significantly more computational effort and is not needed for the purpose of calculating the waterjet performance indicators such as net thrust and system efficiency (Bulten & Van Esch, 2007). The simulations are carried out over a range of ship speed at different IVR ratios for the waterjet. The control volume analysis used for the powering performance predictions in the towing tank test is replicated to get the net jet system thrust.

Current verification and validation (V&V) work is performed as a prerequisite to identify the opportunity of URANS based global design optimization of waterjet intake duct shape (Takai, 2010). URANS based global

optimization has been successfully demonstrated and validated recently for high-speed sealifts, but without waterjet propulsion (for instance, Tahara *et al.*, 2008, Campana *et al*., 2009). Since one of the main focuses of the current optimization endeavor is the optimization of the waterjet inlet geometry with regards to hull interaction and stern forces, a detailed validation of the prediction capability of URANS for high-speed waterjet propelled sea-lifts is necessary.

2. Computational method (CFDSHIP-IOWA V.4)

The Unsteady Reynolds-Averaged Navier Stokes (URANS)/ Detached Eddy Simulation (DES) flow solver, CFDSHIP-IOWA has been developed at IIHR –Hydroscience & Engineering– over the past 15 years for ship hydrodynamics applications (Xing *et al*., 2008a, Carrica *et al*., 2007a and 2007b). For the present work, URANS with the blended k-ε/k-ω turbulent model is selected as a flow solver. The free surface location is predicted by a single phase level set method. A second order upwind scheme is used to discretize the convective terms of momentum equations for URANS. A pressure-implicit split-operator (PISO) algorithm is used to enforce mass conservation on the collocated grids. The pressure Poisson equation is solved using the PETSc toolkit (Belay *et al.*, 2002). All the other systems are solved using an alternating direction implicit (ADI) method. For a high performance parallel computing, a MPI-based domain decomposition approach is used, where each decomposed block is mapped to one processor. The code SUGGAR (Noack, 2005) runs as a separate process from the flow solver to compute interpolation coefficients for the overset grids and communicates with a motion controller (6DOF) within CFDSHIP at every timestep. The software USURP (Boger and Dreyer, 2006) is used to compute area and forces on the surface overlapped regions. In addition, a simplified body force model is used for waterjet propelled simulation to prescribe axisymmetric body force with axial and tangential components (Paterson *et al.*, 2003). The propeller model requires thrust, torque, and advance coefficients as input and provides the torque and thrust forces. These forces appear as a body force term in the momentum equations for the fluid inside the propeller disk. The location of the propeller is defined in the static condition of the ship and moves according to the ship motions.

3. Simulation design

The simulations are carried out on a 1/34 scale model for the 970 ft long JHSS ship, replicating the experimental model testing. EFD data includes resistance, sinkage and trim for both the barehull and waterjet appended hull. In addition, detailed data for the waterjet propelled hull including thrust deduction, self-propulsion thrust, waterjet inlet boundary layer measurements, waterjet volume flow rate, and velocity measurements at different stations inside the duct are available. The ship is modeled at a full scale forward speed of 36 knots, and the corresponding Froude Number (Fn) is 0.34. The overall uncertainty intervals were estimated by 5.79%, 3.84%, and 0.12% at

Fn=0.34 for delivered horse power, thrust deduction, and ship speed respectively. A Monte Carlo method was used to determine both the sensitivity and uncertainty intervals.

For barehull resistance computations, the ship is initially static on calm water. The ship is then allowed to pitch and heave under a constant inlet fluid velocity until a steady state is reached. Ship-fixed coordinate system is used, which means that there is no surge motion allowed for the ship and the background grid. For self-propulsion simulation, an actuator disk model is used to prescribe axisymmetric body force with axial and tangential components. During simulations, the ship accelerates until the resistance equals the prescribed thrust and added tow force and converges to the self propulsion point (SPP). 2-5 nonlinear iterations are required for convergence of the flow field equations within each time step. Convergence of the pressure equation is reached when the residual imbalance of the Poisson equation drops six orders of magnitude. All other variables are assumed convergence when the residuals drop to 10^{-3}.

Figure 3(a) and 3(b) show the grid topologies with domain and boundary conditions for barehull and waterjet designs, respectively. Body-fitted "O" type grids are generated around ship hull geometry. The barehull grid consists of 3 blocks; namely, fore-hull, aft-hull, and background block. A rectangular background grid is used with clustered grid near the free surface to resolve the wave field. In addition, the waterjet grid makes extensive use of overset grids, and consists of 18 blocks in order to express complicated waterjet geometry accurately. In the present work, the shaft and the downstream rotor are not included in order to avoid the complexity of the grid design since the present work is prerequisite for optimization work. For self propelled simulations, a total of 13 million grid points (fine case) is split into 120 blocks with an average of 105K grid points/block by the MPI based domain decomposition. For both simulations, only half domain is computed taking advantage of the symmetry of the problem and the simulation domain is extended to [-0.5, 2.5], [-0.7, 0.7], [0, 1.3] in streamwise, spanwise and normal directions, respectively. The boundary conditions are detailed in Table 1.

4. Verification and Validation analysis

Methodology and procedure

The uncertainty assessment study is conducted for both JHSS barehull resistance and waterjet propelled simulation following the quantitative methodology and procedures proposed by Stern *et al.,* (2006a) and recently proposed factor of safety method by Xing and Stern (2010), which are effective approaches to guarantee the accuracy and quality of the numerical solutions from CFD simulations quantitatively. Verification is a process for estimating the most important numerical error sources such as iterative error δ_I, grid size error δ_G and time-step error δ_T, and provides error and uncertainty estimates of simulation numerical uncertainty U_{SN}. Validation methodology and procedures use benchmark experimental data D and properly take into account both U_{SN} and experimental uncertainty U_D in estimating modeling errors and validation uncertainty U_V. The U_{SN} is estimated based on

graphical methods for iterative uncertainty U_I and generalized Richardson extrapolation for grid-size uncertainty U_G and time-step uncertainty U_T, and is expressed as;

$$U_{SN}^2 = U_I^2 + U_G^2 + U_T^2 \tag{1}$$

The comparison error $|E|$ is defined by the difference between D and simulation values S as $|E| = |D - S|$. The U_V is defined as;

$$U_V = \sqrt{U_{SN}^2 + U_D^2} \tag{2}$$

When the error $|E|$ is within $\pm U_V$, solutions are validated at the levels of U_V.

It is assumed that iterative convergence has been achieved such that the iterative uncertainty is one order-of-magnitude smaller than the grid-size and time-step uncertainty. The uncertainty estimates for Grid/time-step convergence studies are conducted with multiple solutions using systematically refined grid sizes or time steps with constant refinement ratio. First, refinement ratio r for grid/time is selected. As an example, taking 3, 2, and 1 represent coarse, medium, and fine grids with grid spacing Δx_3, Δx_2, and Δx_1 respectively. The refinement ratio between these solutions is defined as $r = \frac{\Delta x_2}{\Delta x_1} = \frac{\Delta x_3}{\Delta x_2}$. If S_1 represents the solution from fine grid, S_2 from medium, and S_3 from coarse grid, solution change ε for medium – fine and coarse – medium solutions and the convergence ratio R are defined by;

$$\varepsilon_{21} = S_2 - S_1 , \qquad \varepsilon_{32} = S_3 - S_2 , \qquad R = {}^{\varepsilon_{21}}/_{\varepsilon_{32}} \tag{3}$$

Convergence types are defined by following four conditions based on the value of R;

a)	Monotonic Convergence (MC):	$0 < R < 1$
b)	Oscillatory Convergence (OC):	$R < 0 \ and \ \ |R| < 1$
c)	Monotonic Divergence (MD):	$R > 1$
d)	Oscillatory Divergence (OD):	$R < 0 \ and \ \ |R| > 1$

Errors and uncertainties cannot be evaluated for divergence condition (c) and (d). For oscillatory convergence (b), uncertainty can be evaluated based on the determination of the upper S_U and lower S_L bounds of solution oscillation $U_{SN} = (S_U - S_L)/2$. When the solutions achieved monotonic convergence (a), generalized Richardson Extrapolation (RE) can be used to estimate order-of-accuracy p_{RE} as following equation.

$$p_{RE} = \frac{ln\left({\varepsilon_{32}}/{\varepsilon_{21}}\right)}{ln(r)} \tag{4}$$

Herein, the ratio of p_{RE} to p_{th}(theoretical order of accuracy of the numerical solver) is used to show the distance from the asymptotic range which is $P = \frac{p_{RE}}{p_{th}}$. In the present work, p_{th} is set to 2 since the order of accuracy is 2nd order. The simulation numerical uncertainty U_{SN} is estimated based on the following equations;

$$U_{SN} = \begin{cases} (2.45 - 0.85P)|\delta_{RE}| & 0 < P \leq 1 \\ (16.4P - 14.8)|\delta_{RE}| & 1 < P \end{cases} \tag{5}$$

<u>Results of V&V analysis for JHSS</u>

Extensive verification and validation studies are conducted for JHSS with two degrees of freedom (pitch and heave) at the design cruise speed (Fn=0.34, Rn=2.78×10^7). As summarized in Table.2, two sets of triplet grid systems (1,2,3 and 2,3,4) are generated by systematically refined from coarse grid using refinement ratio $r_G = \sqrt{2}$ for barehull resistance simulation cases; whereas, one set of triplet grid systems (1W,2W,3W) are prepared for waterjet cases. The total grid points and corresponding Y+ values are detailed in Table 2. Simulations for grid-size convergence study are performed using time step size $\Delta t = 0.010\ L/U_0$. In the present CFD simulation, friction and pressure stresses in the axial direction are integrated over the surface area of the JHSS and summed to yield the total resistance coefficient. The integration is performed in post processing using a second-order accurate method based on the trapezoidal rule. Verification variables are the integral quantities; total drag coefficient (C_t), frictional drag coefficient (C_f), pressure drag coefficient (C_p), dynamic sinkage, and dynamic trim. For the self propulsion simulations, the ship accelerates until the resistance equals the prescribed thrust and added tow force and converges to the self propulsion point (SPP); therefore, force coefficients investigated for barehull case become prescribed constant variables. As a result, verification study is done on SPP and dynamic motions for waterjet case. In the following sections, the detailed solutions and corresponding discussions are presented for both JHSS barehull and waterjet appended hull; and the solutions are shown in Table 3, 4 and Figure 4.

<u>Barehull resistance simulation at design speed</u>

Parametric studies on the nonlinear iterations for each time step ensure iterative convergence at each time step. Results show that by increasing the nonlinear iterations from 3 to 5, the difference for the resistance coefficient C_t is less than 0.1%; thus, the iterative error depending on the number of inner iteration can be considered to be negligible. Additionally, U_I are of the same order of magnitude for all grids, which suggests that it is mainly determined by the iterative method applied and independent of grid resolutions. Usually, the quantitative estimates of iterative uncertainty U_I (oscillation/fluctuation of the running mean) are not given since it is small compared to grid uncertainty; however, it turns out that some of these values are big (especially

waterjet case); thus, they are also presented in the following tables. The grid convergence study is conducted using a grid refinement ratio $r_G = \sqrt{2}$, and Table 3 summarizes the solutions of the resistance coefficients and ship motions obtained from barehull resistance computations with experimental uncertainties. As summarized Table.3, U_I is negligibly small, average of 0.23%S (where S is solution on finest grid). Corresponding U_I/ε_{12_G} values for grids (1,2,3) are 0.5, 0.3, and 0.01 for C_t, sinkage, and trim, respectively. These small values (< 1) indicate that the U_G is not affected by U_I. The convergence ratios (R_G) show the predicted convergence type (Eq. 5). All force coefficients; namely, C_t, C_f, and C_p, show monotonic convergence with average of R_G=0.65. Dynamic trim also show monotonic convergence, whereas the sinkage with grids (2,3,4) shows divergence. Overall, mostly monotonic convergence is obtained for the verification variables in this study. The order of accuracy ($P_G = p_{RE_G}/p_{th}$) differ 0.4 to 1.4. Most importantly, both grid-triplet studies achieve monotonic convergence for the total resistance coefficient (C_t) at the reasonable grid uncertainties (~3.5%S). For the sinkage, the solution from grid (1,2,3) achieves monotonic convergence with U_G=0.9%S; however, the ones from grids (2,3,4) show divergence such that U_G cannot be estimated. For trim, U_G is assessed at the average interval of 23.8%S which is relatively big uncertainty. The reason why the trim uncertainties get large is the fact that the absolute values are quite small (closer to zero) in this particular simulation case; and it is typical that motions are more difficult to converge in grid, compared to resistance (Xing *et al.*, 2008a). Overall, U_G for all the verification variables on grids (1,2,3) show smaller values than ones on grids (2,3,4) which is reasonable in consideration of the overall number of grid points.

Since steady-state simulations are performed for barehull resistance computations, the time step convergence study is not performed. The simulation numerical uncertainty $U_{SN} = \sqrt{U_I^2 + U_G^2}$, experimental data uncertainty U_D, validation uncertainty U_V, and comparison error $|E| = |D - S|$ are included in Table 3. Eventually, E is bigger with the higher resolution grid set (for C_t) than the lower; however, both values are of acceptable accuracy (~2.5%D). For grids (1,2,3), $E < U_V$ such that C_t is validated at the interval of U_V=6.5%D. Reducing intervals of validation uncertainty for C_t primarily requires reduction in experimental uncertainties since U_D=5.8%D > U_{SN}=3.6%D. Due to the lack of experimental data for the motions, U_{SN} is used as the validation uncertainty. Dynamic trim is validated on finer grid set for which E=13.8%D < U_{SN}=21.2%D; whereas the sinkage is not validated since E=11.6%D > U_{SN}=0.7%D. Trim is validated but at the larger validation uncertainty interval due to larger U_G.

<u>Waterjet propelled simulation at design speed</u>

Table 4 summarizes the V&V analysis for waterjet propelled computations. All the necessary information is shown with same manner as barehull resistance simulation results. As mentioned earlier, U_I show bigger values (average of 2.8%S) than ones for barehull case (average of 0.2%S), and these are not negligible for waterjet case. It would indicate that waterjet simulations need longer iterations to get convergence than barehull case due to flow complexity. As a result, corresponding U_I/ε_{12_G} values show bigger values for motions. The reason why U_I/ε_{12_G} for SPP gets bigger is different; and it is because ε_{12_G} is relatively small (about 0.14%S). According to R_G values, all the

investigated variables achieve the convergence (monotonic or oscillatory type). Oscillatory convergence is predicted for SPP, which is not strong convergence type; in contrast, dynamic motions achieve monotonic convergence. The order of accuracy ($P_G = p_{RE_G}/p_{th}$) for motions is average of 0.7. U_G for motions show relatively large uncertainties (U_G >14%S); on the other hand, U_G for SPP show reasonable uncertainties (U_G~1.1%S). All the solutions for both barehull and waterjet grids with EFD values are presented in Figure 4. The grid convergence is clearly seen from the figure as well.

The simulation numerical uncertainty U_{SN}, experimental data uncertainty U_D, validation uncertainty U_V, and comparison error $|E|$ for waterjet simulations are shown in the rest columns of Table 4. Note that the errors for dynamic sinkage and trim shown in Table 4 are obtained at different speed; thus, the displayed EFD values are obtained by interpolating the original data set. For the SPP, $E < U_V$ such that SPP is validated at the U_V=1.1%D interval but with oscillatory convergence condition. Dynamic trim and sinkage are validated for which E=10.3%D < U_{SN}=14.4%D and E=27.4%D < U_{SN}=28.5%D, respectively. These are relatively large than the ones for barehull simulation and it is difficult to get stable convergences for the self-propulsion simulations due to the complexity of waterjet flow with dynamic motions.

<u>Resistance and motion curves over the speed range</u>

The CFD results of resistance, dynamic trim, and sinkage over a speed range of 18-42 knots are shown with EFD data and uncertainties U_D in Figure 5. Total resistance (R_t) curve and corresponding thrust deduction ($R_{t_{BH}}/R_{t_{WJ}}$) are presented in Figure 5(a). EFD resistance increases with the speed and it does not yet reach hump within the available data for both barehull and waterjet designs. Predictions of CFD computations capture the general trend, and show reasonable agreement with EFD within the average errors of 1.8%D and 8.0%D over the speed range for barehull and waterjet case, respectively. In particular, the errors from EFD are 0.12%D(BH) and 6.9%D(WJ) at the design cruise speed. EFD thrust deduction differs 0.88 to 0.96, and there is slight change in speed except lower speed case. CFD captures the trend of thrust deduction change; however, it overestimated with the average of 8.5%D. At the design speed, the error is overestimated by 7.5%D; this is due to the underpredicted waterjet resistance and overpredicted barehull resistance.

Dynamic motions for pitch and heave are predicted in running conditions and the curves over speed range are shown in Figure 5(b). EFD sinkage increases constantly with Fn, and waterjet induced effect is seen quite small. The dynamic trim shows a bow down trend which reaches a minimum value at 36 knots for both cases, and then follows a bow up trend. Waterjet induced effect is seen on trim; but it seems constant in speed. CFD computations capture the trend of EFD trim and sinkage over the speed range with reasonable accuracy for barehull case. For waterjet simulations, CFD trim captures the trend qualitatively; however, it underpredicted quantitatively with the average of 21%D. Since trim show closer to zero for some speeds, the comparison error is taken by the dynamic range of EFD data, which is 0.175 and 0.260 for barehull and waterjet case, respectively. The prediction of CFD

sinkage agrees properly with EFD qualitatively but overpredicted about 12%D. The average errors over the speed range are summarized in Table 5.

Verification of point variables for barehull resistance simulations

Figure 6 shows the global wave fields for barehull resistance computations at Fn=0.34. Free surface elevations and mean wave are compared between four grid systems. As shown in the Figure 6(a), solutions from higher resolution grids well capture general free surface feature such as Kelvin wave pattern with about 20° of envelope half angle. These plots clearly show the grid convergence as well as the quantitative value obtained in the previous section. The results from waterjet propelled computations show similar trends of these wave fields depending on the grid resolutions; thus, these figures are not presented in this paper. Verification study of point variable is conducted for mean wave profiles. The computed wave height at the intersection of the free surface and no-slip surface from $0 \leq x/L \leq 1$ defines the wave profiles and solutions on four different grid systems are compared in Figure 6(b). Iteration errors and uncertainties are found to be negligible in comparison to the grid convergence for all solutions, i.e., $U_I \ll U_G$ such that $U_{SN} = U_G$. Evaluation of convergence ratio R_G and order of accuracy P_G for point variables can be problematic when solution changes $\varepsilon_{G_{21}}$ and $\varepsilon_{G_{32}}$ both go to zero so that their ratio is ill-defined. To overcome this problem, separate L2 norm of $\varepsilon_{G_{21}}$and $\varepsilon_{G_{32}}$ are used to define ratios for R_G and P_G. Table 6 tablets the investigated grid set, profile-averaged R_G, P_G, and global grid uncertainty U_G. Monotonic convergences are obtained for both grid sets with average interval of U_G=2.3%S; however, with $\langle p_G \rangle$ less than p_{th}. Noteworthy, $\langle U_{G123} \rangle \leq \langle U_{G234} \rangle$ is obtained which means the convergence is achieved with corresponding grid refinement. EFD data did not give the information for wave profiles; hence, the validation study is not conducted yet.

5. Performance analysis of waterjet propelled simulations

The waterjet propelled simulations are conducted over a range of prescribed thrust, obtained using shaft dynamometers in the EFD, and the speed is predicted. The error in predicted speed is less than 8%D over the range of prescribed thrust with Grid #2W. The prescribed shaft thrust is not an indication of the net jet thrust, which is calculated using the ITTC control volume approach. The inlet (St. 1) and the streamlines for the CFD control volume are shown in Figure 7(a), for Fn=0.34 simulation case. The velocity profiles at the inflow capture area and the exit are shown in Figure 7(b). The width of the capture area varies with speed and has the highest width and therefore highest boundary layer ingestion at 35 knots. The dynamic trim shown in Figure 4(b) correlates with Figure 7(b); minimum trim occurs at 35 knots, indicating that the boundary layer ingestion is related to the trim.

The volume flow rate (VFR) obtained by integration of the velocity field at St. 6 shows a good agreement with EFD with an average error of 5.6%D over the speed range (Figure 8). The inlet wake fraction (IWF) calculated at St. 1 is also compared with EFD in Figure8. The lowest wake fraction occurs at speed corresponding to the

highest boundary layer ingestion and lowest trim. URANS simulation captures general trend of IWF as well as VFR. The average error of IWF over the speed range is 2.7%D. Note that the EFD assumes a trapezoidal capture area of the same width but differing heights for calculations of the inlet wake fraction. This difference of definition contributes to the error since the momentum flux method greatly depends on the shape and size of the capture area (St. 1). URANS can be a useful tool in estimating more realistic capture area by tracing back streamlines entering the rotor to an upstream slice plane, which is also discussed in Delaney *et al.*, (2009).

The net jet thrust is obtained by the momentum flux approach recommended by ITTC. The momentum and energy at St. 1, 3 and 6 are integrated at any station *N* using Equations (6) to (8).

$$M_N = \rho \bar{V}_N^2 \int_{A_N} \left(\frac{V_{Ex}}{\bar{V}}\right)_N \times \left(\frac{u_x}{\bar{V}}\right)_N \times dA_N \tag{6}$$

$$E_N = \rho \bar{V}_N^3 \int_{A_N} \left(\frac{V_{Ex}}{\bar{V}}\right)_N^2 \times \left(\frac{u_x}{\bar{V}}\right)_N \times dA_N \tag{7}$$

where the energy velocity V_E includes the static pressure and velocity terms;

$$\frac{1}{2}\rho (V_E)^2 = \left(\frac{1}{2}\rho u^2 + p\right) \tag{8}$$

The momentum flux at St. 1 and 6 are shown in Figure 9(a) together with net jet thrust which is the difference of momentum flux from St. 1 to 6. The average error of net jet thrust is 6.5%D. The inlet efficiency is a measure of losses incurred from flow entering the waterjet inlet, and it is obtained by calculating the energy at St. 1 and 3 (Figure 9(b)). The error in the inlet efficiency is mainly due to the difference in the energy calculations between CFD and EFD at St. 3. EFD uses 4 pressure taps at the circumference of the duct in the energy calculations, whereas the CFD averages the pressure over the whole cross section. The average error of inlet efficiency over the speed range is 7.4%D. CFD results show underestimated value of inlet efficiency as well as energies at St. 1 and 3.

EFD inlet efficiency shows significant losses (>15%) over the speed range; frictional drag and pressure losses through the duct are combined together to make losses bigger. Herein, the opportunity of design optimization for intake duct shape can be identified; that is, to maximize the inlet efficiency by geometrical modification. Improving inlet efficiency can be paraphrased to reduction of powering requirement. Furthermore, the self-propelled speed at a given thrust can be used to gauge the powering performance; the shaft thrust requirements are obtained from speed-thrust relations, and it is detected that ~1% increase in speed requires ~4% increase in shaft thrust at the design speed in the present work.

The jet interface with the wake is well captured by URANS (Figure 10(a)). The outboard nozzle discharge quickly buries into the flow around the transom creating the characteristic “W” shape in both EFD and CFD clearly.

All cases have circumferential variation in pressure, both before and after the nozzle even without swirl as an effect of intake geometry. Figure 10(b) compares the boundary layer and free surface elevation between the self-propelled case and the barehull towed simulations. The free surface wake just past the transom is slightly altered due to the jet discharge.

URANS computations are compared to experimental LDV measurements at a model scale. Figure 11 shows the comparison of the flux parameters at St. 3 and 6 for the Fn=0.34 case. The non-uniformity of the flow is captured well at St. 3 which shows a higher mass flux at the lower half compared with the top region. EFD shows a significant swirl effects in not only St. 3 but also St. 6 due to the blade and shaft inside the duct which are not modeled in CFD; however, simulation captures the lower mass flux at the center and higher one near the circumference. The boundary layer thicknesses at St. 1 are presented at both inlet open and closed situations at Fn=0.34 (Figure 12). The bulges in the boundary layer at St. 1 seem both in CFD and EFD causes difference in intake between the inner and outer waterjet. CFD results show no variation of streamwise velocity along the hull width; on the other hand, EFD indicate that the boundary layer thickness changes in the vicinity of the ship centerline (Y=0).

6. Conclusion and future work

URANS simulations for both barehull and waterjet propelled JHSS are presented. CFDSHIP-IOWA V.4 is employed as a flow solver, which solves URANS with the blended k-ε/k-ω turbulent model, single-phase level set method, and simplified body force model are adopted to simulate the waterjet propelled ship flow. The present work is performed for following purposes; namely, 1) to investigate the capability of URANS flow solver to the accurate powering prediction of waterjet propelled simulation including the waterjet-hull interactions; 2) to carry out detailed verification and validation (V&V) analysis; and 3) to identify the optimization opportunity for intake duct shape design. Main focuses of investigation in this paper are put on uncertainty analysis of both barehull and waterjet appended hull and detailed performance analysis of waterjet propelled simulations.

The present work demonstrates the feasibility of using URANS for performance analysis of hull-integrated waterjet propelled ship with free surface and dynamic motions. A verification study is conducted for barehull simulations by four systematically refined grids ranging from 1.2×10^6 to 28×10^6 grid points, which allows two sets of grid studies; on the other hands, it is done for waterjet case by three systematically refined grids. Uncertainty intervals of iterative/grid size convergences are assessed, and the solutions are validated at the design speed (36knots). Ultimately, total resistance coefficient (C_t) for barehull is validated at the average interval of 7.0%D and ship speed for self-propulsion simulation is validated at the uncertainty interval of 1.1%D. In addition, predictions of CFD computations capture the general trend of resistance over the speed range of 18-42knots, and show reasonable agreement with EFD within the average errors of 1.8%D and 8.0%D for barehull and waterjet case, respectively. CFD computations capture trends of EFD motions over the speed range with reasonable accuracy. For

barehull simulation, the verification of point variables for wave profiles is also performed, and the grid uncertainty shows reasonable intervals (average of 2.3%S). Overall, the validation is achieved at reasonable uncertainty intervals and URANS captures the important trends of force and motions properly; thus, the current V&V work has proved that the present URANS approach is an accurate tool to predict the resistance of both JHSS barehull resistance and waterjet computations.

Detailed flow parameters for waterjet propelled simulations are also investigated. Overall, the main performance parameters; namely, net jet thrust, inlet efficiency are predicted reasonably well with an accuracy of ~10%. The simulation using URANS with simplified body force model captures jet wake interference structures well, and warrants more studies into the jets effect on ship wake signatures. Certain issues need to be addressed further to improve validation of the detailed flow features within the duct; both the shaft and the downstream rotor induce some swirl at the inlet St. 3 and 6, which has been neglected. The actuator disk model provides a pressure jump in the axial direction; however, it does not account for the swirl effects due to the blade-rotating. It might cause the increase in error with increase in loading for the shaft thrust. The effects of blades and shafts are needed to be investigated numerically. Additionally, detailed CFD waterjet modeling of geometry including blade-rotating needs to be considered to achieve more realistic simulation.

This work paves way for waterjet inlet optimization studies. The main objective of the optimization is to decrease powering requirements by increasing the inlet efficiency through modification of intake duct shape, which currently shows significant losses (> 15%) over the speed range. Detailed flow diagnostics of pressure variations, secondary cross flows, and turbulence flows inside the duct would uncover the mechanisms of energy loss and guide shape optimization. The arrangement of the intake ducts could also be optimized. Initial optimization would focus on modification of intake duct shape to maximize inlet efficiency at 36knots, followed by optimization for modification of whole hull with multiple speeds. Additionally, the bow shape can be optimized since the unique “gooseneck” bow is selected for JHSS model.

Acknowledgments This work is sponsored by the US Office of Naval Research through research grants N00014-08-0491, under the administration of Dr. Ki-Han Kim. The simulations were performed on 4.7GHz IBM Power 6 machine ‘*DaVinci*’ at the DoD NAVO center.

References

1. Balay, S., Buschelman, K., Gropp, W., Kaushik, D., Knepley, M., Curfman, L., Smith, B. and Zhang, H., (2002) ‘PETSc User Manual,’ ANL-95/11-Revision 2.1.5, Argonne National Laboratory
2. Bulten, N.W.H. & Van Esch, B.P.M. (2007) ‘Fully transient CFD analyses of waterjet pumps’, Marine Technology, 44(3), pp. 185-193
3. Bulten, N.W.H. (2006). ‘Numerical Analysis of Waterjet Propulsion System’, PhD thesis, Technical University of Eindhoven, ISBN-10: 90-386-2988-5. Library Eindhoven University of Technology

4. Boger, D.A. & Dreyer, J.J. (2006) 'Prediction of Hydrodynamic Forces and Moments for Underwater Vehicles Using Overset Grids', AIAA paper 2006-1148, 44th AIAA -Aerospace Sciences Meeting, Reno, Nevada, 2006
5. Campana, E. F., Peri, D., Tahara, Y., Kandasamy, M., and Stern, F. (2009) 'Numerical Optimization Methods for Ship Hydrodynamic Design', Society of Naval Architects and Marine Engineers 2009 Annual Meeting and Expo
6. Carrica, P. M., Wilson, R. V., and Stern, F. (2007a) 'An unsteady single-phase level set method for viscous free surface flows' International Journal for Numerical Methods in Fluids, Vol. 53, pp. 229-256
7. Carrica, P. M., Wilson, R. V., Noack, R., and Stern, F. (2007b) 'Ship motions using single-phase level set with dynamic overset grids', Computers and Fluids, Vol. 26, pp.1415-1433
8. Carrica, P. M., Wildon, R. V., Noack, R., Xing, T., Kandasamy, M., Shao, J., Sakamoto, N., and Stern, F. (2006) 'A Dynamic Overset, Single-Phase Level Set Approach for Viscous Ship Flows and Large Amplitude Motions and Maneuvering', 26th symposium on Naval hydrodynamics, Rome, Italy
9. Delaney, K., Donnely, M., Elbert, M., and Fry, D. (2009) 'Use of RANS for Waterjet Analysis of a High-Speed Sealift Concept Vessel', 1st International Symposium on Marine Propulsors, Trondheim, Norway
10. Hino, T., Ohashi, K. (2009) 'Numerical Simulation of Flow around a Waterjet Propelled Ship' 1st International Symposium on Marine Propulsors, Trondheim, Norway
11. Jang, J.H., Park, W.G., Boo, J.S., Chun, H.H., & Kim, M.C. (2004) 'Numerical Simulations of Waterjet with Rotor-Stator Interaction', 10th international symposium on transport phenomenon and dynamics of rotating machinery, Hawaii
12. Jessup, S., Donnelly, M., Fry, D., Cusanelli, D., & Wilson, M. (2008) 'Performance Analysis of a Four Waterjet Propulsion System for a Large Sealift Ship', 27th symposium on Naval hydrodynamics, Seoul, Korea
13. Kandasamy, M., Takai, T., Stern, F. (2009a) 'Validation of detailed water-jet simulation using URANS for large high-speed sea-lift', 10th International Conference on Fast Sea Transportation (FAST2009), Athena, Greece
14. Kandasamy, M., Ooi, S.K., Carrica, P., & Stern, F. (2009b) 'Integral force/moment water-jet model for CFD simulations', submitted to Journal of Fluids Engineering
15. Kim, M-C., Chun, H-H., Kim, H. Y., Park, W. K., Jung, U. H. (2009) 'Comparison of waterjet performance in tracked vehicles by impeller diameter', Ocean Engineering, Vol. 36, pp. 1438-1445
16. Lavis, D. R., Forstell, B. G., and Purnell, J. G. (2006) 'Compact Waterjets for High-Speed Ships', 5th International Conference on High Performance Marine Vehicles, Australia
17. Noack, R. (2005) 'SUGGAR: a General Capability for Moving Body Overset Grid Assembly', AIAA paper 2005-5117, 17th AIAA Computational Fluid Dynamics Conference, Toronto, Ontario, Canada
18. Paterson, E. G., Wilson, R. V., and Stern, F. (2003) 'General-Purpose Parallel Unsteady RANS Ship Hydrodynamics Code: CFDSHIP-IOWA', IIHR Technical Report, #432, The University of Iowa
19. Stern, F., Wilson, R., and Shao, J. (2006a) 'Quantitative V&V of CFD simulations and certification of CFD code', International Journal for Numerical Methods in Fluids, Vol. 50, pp. 1335-1355
20. Stern, F., Carrica, P., Kandasamy, M., Gorski, J., O'Dea, J., Hughes, M., Miler, R., Hendrix, D., Kring, D., Milewski, W., Hoffman, R., Cary, C. (2006b) 'Computational Hydrodynamic Tools for High-Speed Sealift', Transactions SNAME, Vol. 114
21. Tahara, Y., Peri, D., Campana, E.F., & Stern, F. (2008a) 'Single and Multi-objective Optimization of a Fast Multihull Ship: Numerical and Experimental Results', 27th Symposium on Naval Hydrodynamics, Seoul, Korea

22. Tahara, Y., Norisada, K., Yamane, M., and Takai, T. (2008b) 'Development and Demonstration of CAD/CFD/Optimizer Integrated Simulation-Based Design Framework by Using High-Fidelity Viscous Free-Surface RaNS Equation Solver', Journal of Japan Society of Naval Architects and Ocean Engineers, Vol. 7, pp. 171-184
23. Tahara, Y., Wilson, R. V., Carrica, P. M., Stern, F. (2006) 'RANS simulation of a container ship using a single-phase level-set method with overset grids and the prognosis for extension to a self-propulsion simulator', Journal of Marine Science and Technology, Vol. 11, pp. 209-228
24. Takai, T. (2010) 'Simulation based design for high-speed sealift with waterjets by high fidelity URANS approach, M.S. thesis, The University of Iowa
25. Van Terwisga, T. *et al.* (2005) 'Report of the Specialist Committee on Validation of Waterjet Test Procedures', Proceedings 24th Int. Towing Tank Conference; II: 471-508
26. Van Terwisga, T. *et al.* (2002) 'Report of the Specialist Committee on Validation of Waterjet Test Procedures', Proceedings 23rd Int. Towing Tank Conference; II: 387-415
27. Wilson, M. B., Gowing, S., Chesnakas, C., & Lin, C-W. (2005) 'Waterjet-hull interactions for sealift ships', International Conference on Marine Research and Transportation (ICMRT'05), Italy
28. Xing, T., & Stern, F. (2010) 'Factors of Safety for Richardson Extrapolation', submitted to Journal of Fluids Engineering
29. Xing, T., Carrica, P. M., and Stern, F. (2008a) 'Computational Towing Tank Procedures for Single Run Curves of Resistance and Propulsion', Journal of Fluids Engineering, Vol. 130, 101102, pp. 1-14
30. Xing, T., & Stern, F. (2008b) 'Factors of Safety for Richardson Extrapolation for Industrial Applications', IIHR Technical report, No. 466, University of Iowa

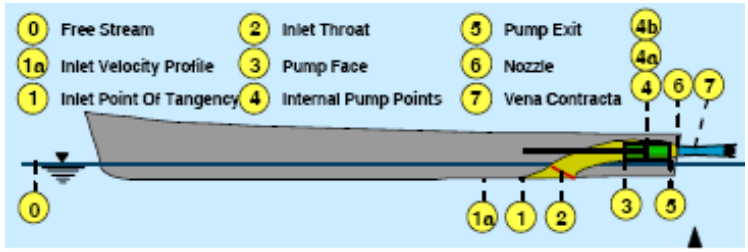

Figure 1: ITTC definitions of analysis control volume and stations

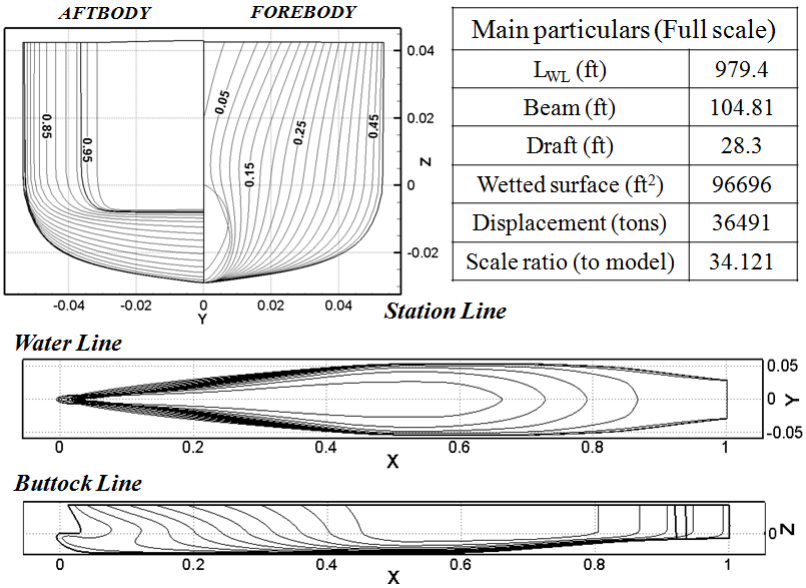

Main particulars (Full scale)	
L_{WL} (ft)	979.4
Beam (ft)	104.81
Draft (ft)	28.3
Wetted surface (ft^2)	96696
Displacement (tons)	36491
Scale ratio (to model)	34.121

Figure 2: Main particulars and lines of JHSS bare hull design

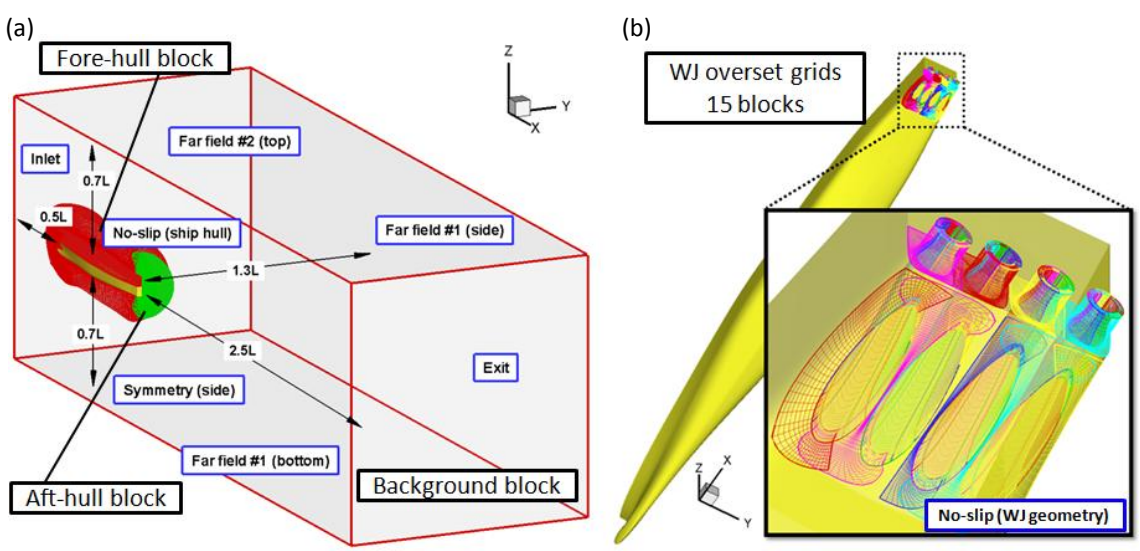

Figure 3: (a) Domain and boundary conditions shown with BH grid, (b) Overset grid design for JHSS WJ model

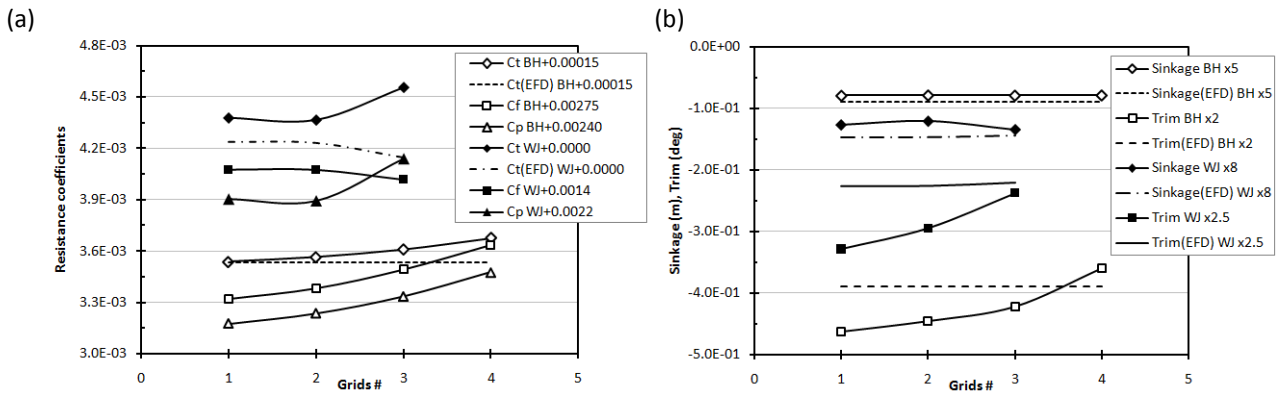

Figure 4: Verification for resistance and motions (Fn=0.34): (a) resistance coefficients, (b) sinkage and trim

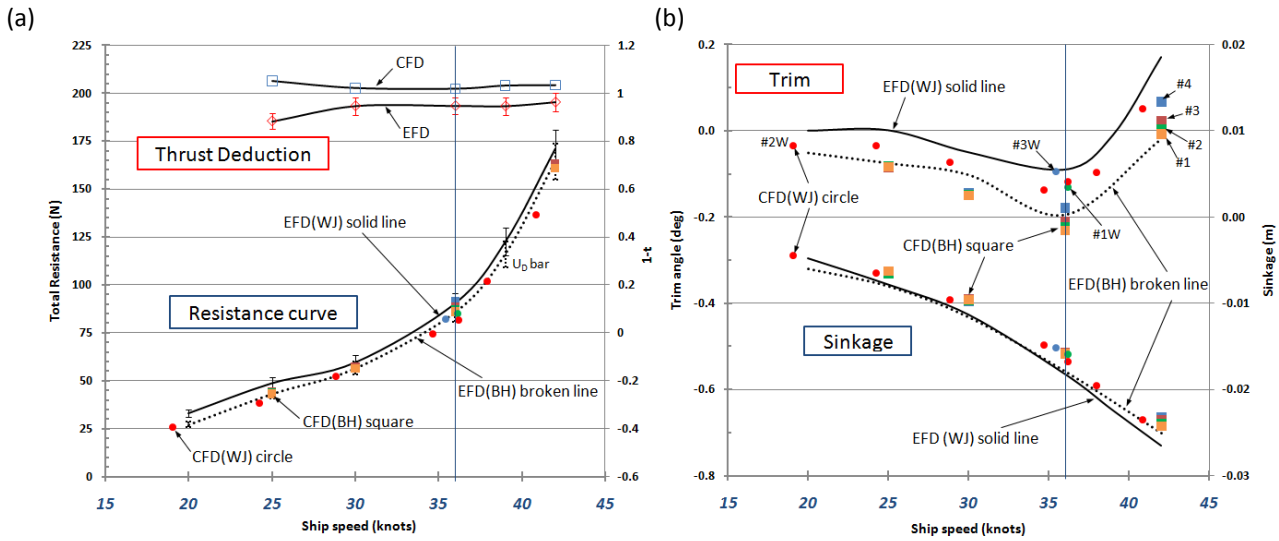

Figure 5: Comparison of forces and motions over speed range of 18-42knots with EFD data:
(a) Total resistance and thrust deduction (b) Dynamic sinkage and trim

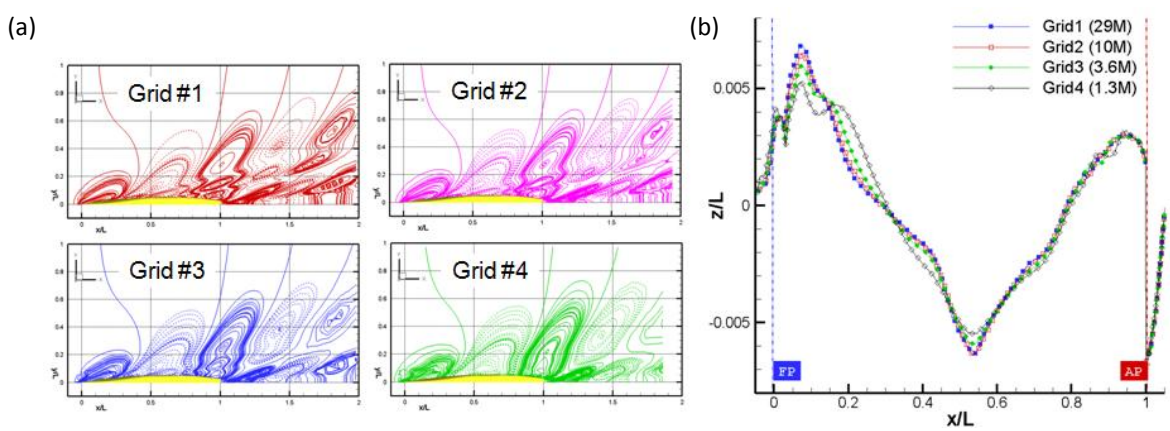

Figure 6: Comparison of wave-fields of JHSS barehull simulations at Fn=0.34
(a) free surface elevations (b) wave profiles

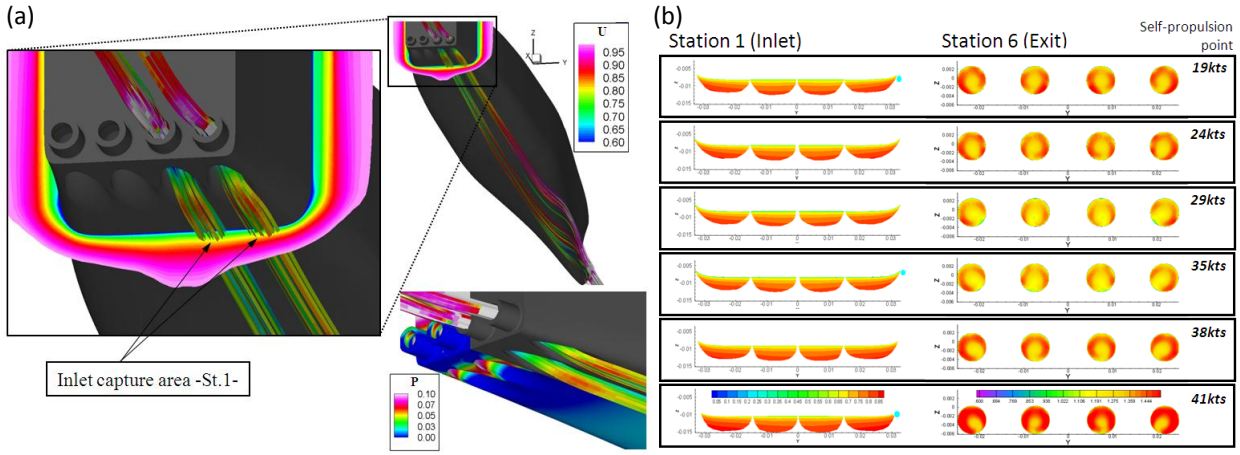

Figure 7: (a) CFD inlet stream tube and velocity profile at station 1 shown with boundary layer and surface pressure
(b) CFD velocity profiles at station 1 and 6 on six different speeds

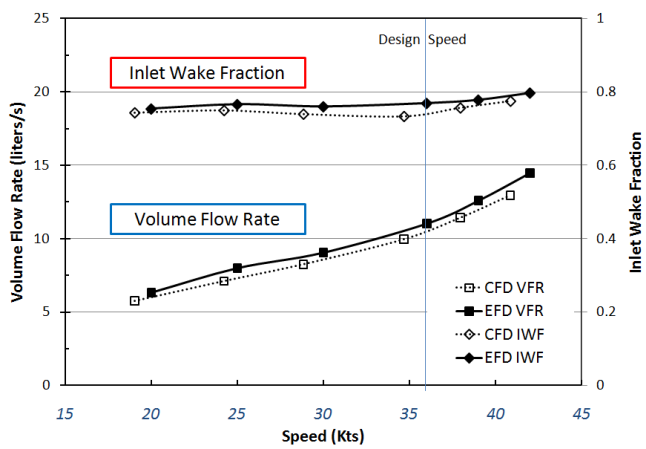

Figure 8: Comparison of volume flow rate at station 6 and inlet wake fraction at station 1

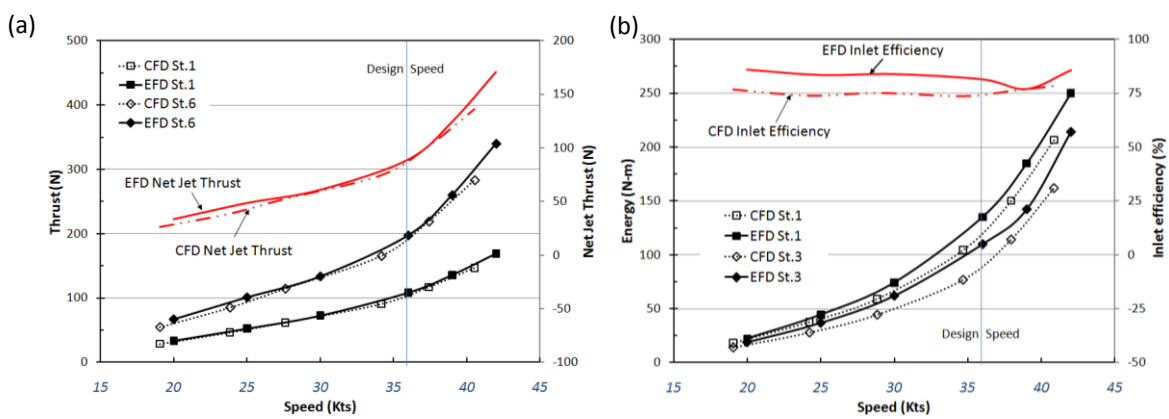

Figure 9: (a) Comparison of momentum flux at station 1 and 6 and net jet thrust
(b) Comparison of energy at station 1 and 3 and inlet efficiency

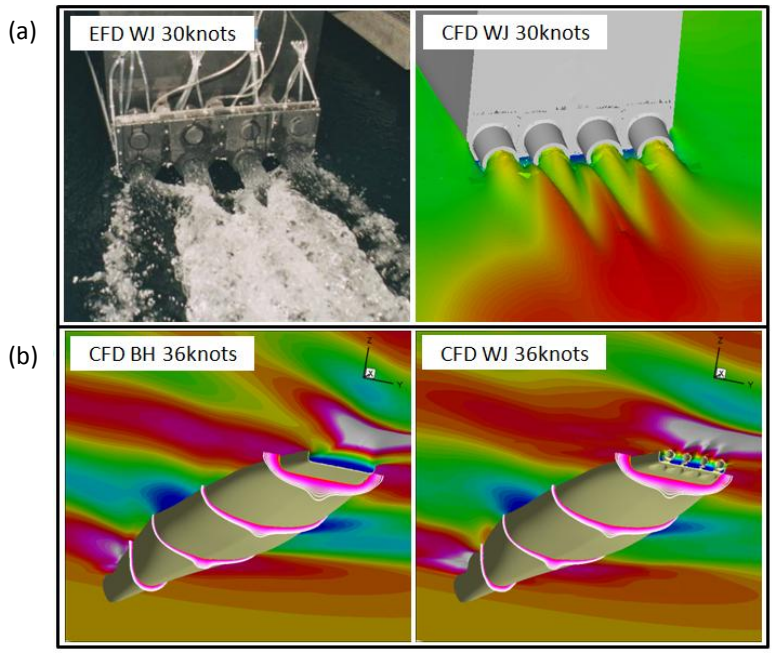

Figure 10: Comparison of (a) jet wake interferences between CFD simulation and EFD
(b) boundary layer and free-surface predictions between BH and WJ propelled simulation

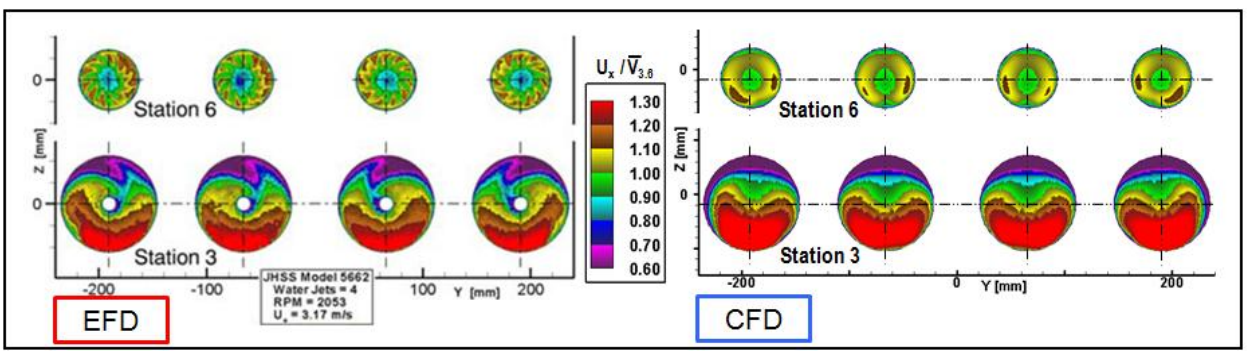

Figure 11 Flux parameters at station 3 and 6 compared with EFD data at 36knots

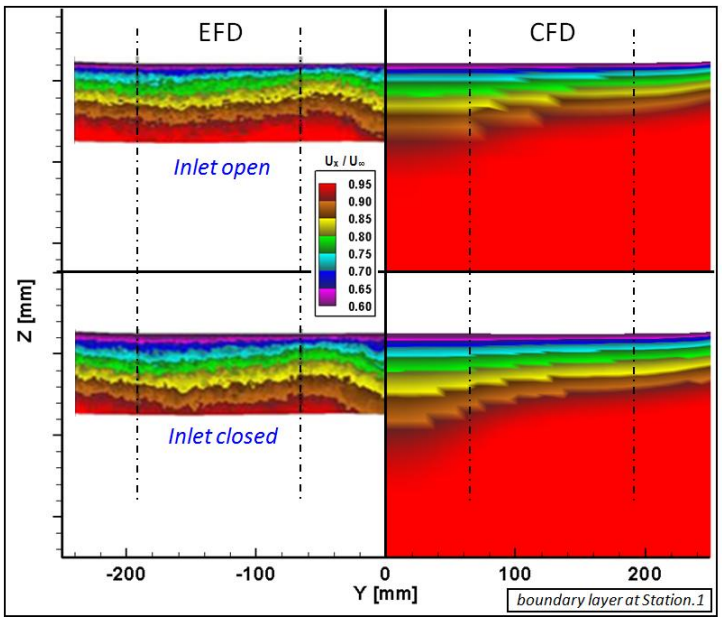

Figure 12 Comparison of boundary layers at station 1 between EFD (Left) and CFD (Right) at 36 knots Inlet open (top) and closed (bottom) condition

Table 1: Boundary conditions

Description		ϕ	p	k	ω	U	V	W
Inlet	Resistance	$\phi = -z$	$\frac{\partial p}{\partial n} = 0$	$k_{fs} = 10^{-7}$	$\omega_{fs} = 9$	$U = 1$	$V = 0$	$W = 0$
	Self-propelled	$\phi = -z$	$\frac{\partial p}{\partial n} = 0$	$k_{fs} = 10^{-7}$	$\omega_{fs} = 9$	$U = 0$	$V = 0$	$W = 0$
Exit		$\frac{\partial \phi}{\partial n} = 0$	$\frac{\partial p}{\partial n} = 0$	$\frac{\partial k}{\partial n} = 0$	$\frac{\partial \omega}{\partial n} = 0$	$\frac{\partial^2 U}{\partial n^2} = 0$	$\frac{\partial^2 V}{\partial n^2} = 0$	$\frac{\partial^2 W}{\partial n^2} = 0$
Far-field #1		$\frac{\partial \phi}{\partial n} = 0$	0	$\frac{\partial k}{\partial n} = 0$	$\frac{\partial \omega}{\partial n} = 0$	$U = 1$	$V = 0$	$W = 0$
Far-field #2		$\frac{\partial \phi}{\partial n} = 0$	$\frac{\partial p}{\partial n} = 0$	$\frac{\partial k}{\partial n} = 0$	$\frac{\partial \omega}{\partial n} = 0$	$U = 1$	$V = 0$	$W = 0$
Symmetry		$\frac{\partial \phi}{\partial n} = 0$	$\frac{\partial p}{\partial n} = 0$	$\frac{\partial k}{\partial n} = 0$	$\frac{\partial \omega}{\partial n} = 0$	$\frac{\partial U}{\partial n} = 0$	$V = 0$	$\frac{\partial W}{\partial n} = 0$
No slip (ship hull)		$\frac{\partial \phi}{\partial n} = 0$	$-$	$k = 0$	$\omega = \frac{60}{\beta Re \Delta y_1^2}$	$\frac{\partial U}{\partial n} = 0$	$V = 0$	$W = 0$

Table 2: Grids information used for verification study of JHSS BH and WJ simulations

#	Description	Total grid points	Y+	#	Description	Total grid points	Y+
1	Finer BH	28,657,743	0.75	1W	Fine WJ	13,077,181	1.13
2	Fine BH	10,150,475	1.13	2W	Medium WJ	6,550,622	1.65
3	Medium BH	3,623,916	1.65	3W	Coarse WJ	4,214,081	2.53
4	Coarse BH	1,278,135	2.53				

Table 3: Verification and validation study for integral variables of JHSS BH (Fn=0.34)

	Grids	U_I†	U_I/ε_{12G}	R_G	P_G	U_G†	U_{SN}†	U_D†	U_V†	E†
Ct	1,2,3	0.167	0.482	0.678	0.561	3.595	3.599	5.79	7.105	2.267
	2,3,4	0.111	0.128	0.608	0.717	3.622	3.624	5.79	6.833	0.897
Cf	1,2,3	0.127	0.062	0.570	0.811	2.740	2.743	-	-	-
	2,3,4	0.051	0.041	0.717	0.358	15.87	15.87	-	-	-
Cp	1,2,3	0.832	0.070	0.611	0.711	22.57	22.58	-	-	-
	2,3,4	0.480	0.062	0.703	0.509	56.50	56.50	-	-	-
Sink	1,2,3	0.214	0.317	0.535	0.903	0.696	0.728	-	-	11.61
	2,3,4	0.137	0.381	-1.654	-	-	-	-	-	11.80
Trim	1,2,3	0.051	0.010	0.732	0.449	21.17	21.17	-	-	13.76
	2,3,4	0.096	0.026	0.378	1.404	26.52	26.52	-	-	4.904

†Note: U_D, U_V and E are %D and others are $\%S_1$ or $\%S_2$

Table 4: Verification and validation study for integral variables of JHSS WJ (Fn=0.34)

	Grids	U_I†	U_I/ε_{12G}	R_G	P_G	U_G†	U_{SN}†	U_D†	U_V†	E†
SPP	1W, 2W, 3W	0.188	1.337	-0.066	-	1.065	1.081	0.12	1.088	0.195
Sink		2.696	0.637	0.637	0.650	14.10	14.36	-	-	10.27
Trim		5.413	0.523	0.598	0.742	28.01	28.53	-	-	27.43

†Note: U_D, U_V and E are %D and others are $\%S_{1W}$

Table 5: Average errors over the speed range between CFD and EFD: all variables are %D

	Rt	*Sinkage*	*Trim*†	*Thrust deduction*	*Volume flow rate*	*Inlet wake fraction*	*Net jet thrust*	*Inlet efficiency*
BH	1.759	11.641	9.293	-	-	-	-	-
WJ	7.987	13.857	21.431	8.523	5.662	2.714	6.506	7.394

†Note: EFD Trim is dynamic range since some of them are close to zero

Table 6: Profile averaged verification results for BH wave profile (Fn=0.34)

	Grids	R_G	P_G	U_G†
Wave profiles	1,2,3	0.536	0.901	1.942
	2,3,4	0.588	0.766	2.569

†Note: U_G is $\%S_1$ or $\%S_2$